

# Correlation between battery material performance and cooperative electron-phonon interaction in $\text{LiCo}_y\text{Mn}_{2-y}\text{O}_4$

Krishna Rao Ragavendran, Prabhat Mandal, and Sudhakar Yarlagadda  
*Saha Institute of Nuclear Physics, HBNI, 1/AF Bidhannagar, Kolkata 700 064, India*  
 (Dated: December 22, 2016)

Understanding the basic physics related to archetypal lithium battery material (such as  $\text{LiCo}_y\text{Mn}_{2-y}\text{O}_4$ ) is of considerable interest and is expected to aid designing of cathodes of high capacity. The relation between electrochemical performance, activated-transport parameters, thermal expansion, and cooperativity of electron-phonon-interaction distortions in  $\text{LiCo}_y\text{Mn}_{2-y}\text{O}_4$  is investigated. The first order cooperative-normal-mode transition, detected through coefficient of thermal expansion, is found to disappear at a critical doping ( $y \sim 0.16$ ); interestingly, for  $y \gtrsim 0.16$  the resistivity does not change much with doping and the electrochemical capacity becomes constant over repeated cycling. The critical doping  $y \sim 0.16$  results in breakdown of the network of cooperative/coherent normal-mode distortions; this leads to vanishing of the first-order transition, establishment of hopping channels with lower resistance, and enhancing lithiation and delithiation of the battery, thereby minimizing electrochemical capacity fading.

## I. INTRODUCTION

Among the commercially available batteries, lithium-ion batteries have the highest energy density and are the primary energy source for portable electronics. The energy stored in rechargeable lithium batteries is limited by their cathodes. Currently, cutting-edge cathodes use either layered  $\text{LiCoO}_2$ , its three-dimensional doped variant  $\text{LiM}_y\text{Mn}_{2-y}\text{O}_4$  (with  $M=\text{Ni}, \text{Co}$ , etc.), or polyanionic compounds such as olivine-type  $\text{LiFePO}_4$  [1–5]. Introduced in 1983 by J. B. Goodenough [6],  $\text{Li}_x\text{Mn}_2\text{O}_4$  serves as an attractive alternative to  $\text{Li}_x\text{CoO}_2$  in terms of environmental friendliness, cost effectiveness, safety [7], as well as with its virtue to enable the variation of the lithium stoichiometry  $x$  over the entire range from 0 to 1. When  $x = 0$ , the battery is said to be in a completely charged state, while  $x = 1$  implies the battery is totally discharged. The material, however, suffers from the problem of electrochemical capacity loss over repeated cycling, which is circumvented by doping at the Mn site with other transition metal atoms [8]. By a trial and error approach, it is established that among the doped variants, the cobalt doped spinel  $\text{LiCo}_y\text{Mn}_{2-y}\text{O}_4$  with doping level between 0.1 and 0.2 is ideal for enhanced battery performance [9–13]. However, to the best of our knowledge, no clear correlation has been made between battery performance and basic physics related phenomena such as structural phase transitions, anomalies in transport and heat capacity, etc. Thus, a detailed understanding of the fundamental physics of  $\text{LiCo}_y\text{Mn}_{2-y}\text{O}_4$  is highly essential for developing cutting-edge energy storage devices.

Phase transitions in  $\text{LiMn}_2\text{O}_4$  (and its doped variants) can be grouped under two categories on the basis of the temperature at which the transitions occur: the high temperature region (200 K to 300 K) involving coherent normal-mode distortions [14] (and charge ordering [15]), and the low temperature region ( $\sim 60$  K) corresponding to the magnetic (i.e., antiferromagnetic) ordering. Phase transitions in the battery material in the former region

(which is close to the room temperature) pertains to a structural transition, is expected to be of significance to the battery performance, and will be studied in this work.

The  $\text{MnO}_6$  octahedra in spinel type  $\text{LiMn}_2\text{O}_4$  are similar to the  $\text{MnO}_6$  octahedra in perovskite manganites (such as  $\text{LaMnO}_3$ ); hence, the framework of coherent normal modes [such as Jahn-Teller (JT) modes] utilized in perovskite manganites is expected to provide insights into normal-mode ordering in the spinel structures. Using experiments and theory, we try to understand the sophisticated physics behind the dopant level of  $\text{LiCo}_y\text{Mn}_{2-y}\text{O}_4$  in the stabilization of cathode materials for energy device applications, so that we can design new materials to transcend the existing performance levels.

In this paper, we investigate transport, structural, and thermal properties of both pure and doped  $\text{LiCo}_y\text{Mn}_{2-y}\text{O}_4$  compounds and examine the effect of these properties on battery performance. We explain the superior electrochemical performance of cobalt-doped  $\text{LiMn}_2\text{O}_4$  within the framework of cooperative-normal-mode physics. When non-JT ions such as  $\text{Co}^{3+}$  replace the JT  $\text{Mn}^{3+}$  ions, the cooperative link connecting the local normal-mode distortions starts to weaken and the electronic conductivity increases due to tunneling of charge carriers through regions of non-cooperative normal modes. As the level of Co reaches a certain threshold (i.e.,  $y \sim 0.16$ ), the cooperative link is completely broken and the electrochemical discharge capacity shows stability with the cycle number. Any further increase in the cobalt level, while ensuring a stable discharge capacity, only contributes to a lowering of the capacity due to a decrease in the number of carriers; this explains the emergence of  $y \sim 0.16$  as the ideal doping level for battery performance.

## II. EXPERIMENTAL PROCEDURES

Spinel type polycrystalline  $\text{LiCo}_y\text{Mn}_{2-y}\text{O}_4$  samples with different values of  $y$  were prepared through a

conventional solid state method. Stoichiometric quantities of  $\text{Li}_2\text{CO}_3$ ,  $\text{MnCO}_3$  and  $\text{CoCO}_3$  were ground and calcined in platinum crucibles at  $800^\circ\text{C}$  for 16 h, with intermittent grindings, in an atmosphere of air. The samples were then pelletized and sintered at  $800^\circ\text{C}$  for 16 h. The phase purity of  $\text{LiCo}_y\text{Mn}_{2-y}\text{O}_4$  samples was checked by high resolution powder x-ray diffraction (XRD) method with Cu  $K_\alpha$  radiation in a Rigaku x-ray diffractometer (TTRAX II). Within the resolution of XRD, we have not observed any peak due to impurity phase(s). The XRD pattern can be indexed well with the space group symmetry  $\text{Fd}3\text{m}$ . Four probe measurements of the electrical resistivity were done in a commercial cryostat (Cryogenic Ltd.) using Keithely 6514 Electrometer. For the thermal expansion measurement, a miniature tilted plate capacitance dilatometer was used. The capacitance has been measured by an Andeen Hagerling 2700A Ultra-precision Capacity Bridge. In this technique, a change in the sample length,  $\Delta L = L(T) - L_0$ , where  $L_0$  is the length of the sample at the lowest measured temperature, can be determined

very accurately. We have measured the macroscopic length change of a sample of dimension 1 mm and the coefficient of linear thermal expansion  $[\alpha(T)]$  has been calculated using the relation,  $\alpha(T) = \frac{1}{L_0} \frac{dL}{dT}$ .

### III. THEORY, RESULTS, AND DISCUSSION

The Hamiltonian for the cooperative electron-phonon interaction system contains the hopping term  $H_t$ , the electron-phonon interaction  $H_{ep}$ , and the lattice term  $H_l$ . Here, in the  $H_{ep}$  term, we consider only the breathing mode (BM) and the JT modes; rest of the normal modes are not taken into account. At the site  $(i, j, k)$ , we define the creation operators for  $d_{x^2-y^2}$  and  $d_{z^2}$  orbitals as  $d_{x^2-y^2;i,j,k}^\dagger$  and  $d_{z^2;i,j,k}^\dagger$ , respectively. The indices  $i, j$ , and  $k$  correspond to labels along the  $x$ -,  $y$ -, and  $z$ -axes, respectively. Next, we express  $H_{ep}$  in the orthogonal basis  $\psi_{x^2-y^2}$  and  $\psi_{z^2}$  as follows [16, 17]:

$$H_{ep} = -\frac{1}{4}g\omega_0\sqrt{2M\omega_0} \times \sum_{i,j,k} (d_{z^2;i,j,k}^\dagger, d_{x^2-y^2;i,j,k}^\dagger) \begin{pmatrix} Q_{x;i,j,k} + Q_{y;i,j,k} + 4Q_{z;i,j,k} & -\sqrt{3}Q_{x;i,j,k} + \sqrt{3}Q_{y;i,j,k} \\ -\sqrt{3}Q_{x;i,j,k} + \sqrt{3}Q_{y;i,j,k} & 3Q_{x;i,j,k} + 3Q_{y;i,j,k} \end{pmatrix} \begin{pmatrix} d_{z^2;i,j,k} \\ d_{x^2-y^2;i,j,k} \end{pmatrix}, \quad (1)$$

where  $g$  is the electron-phonon coupling,  $\omega_0$  is the frequency of optical phonons,  $M$  is the mass of an oxygen ion. Furthermore, we define  $Q_{x;i,j,k} \equiv u_{x;i,j,k} - u_{x;i-1,j,k}$  where  $u_{x;i,j,k}$  and  $u_{x;i-1,j,k}$  are the displacements in the  $x$ -direction of the two oxygen ions along the  $x$ -axis around the site  $(i, j, k)$ ;  $Q_{y;i,j,k}$  and  $Q_{z;i,j,k}$  are defined similarly in terms of the displacements in the  $y$ - and  $z$ -directions of the oxygen ions along the  $y$ - and  $z$ -axes around the site  $(i, j, k)$ , respectively.

Now, the breathing mode  $Q_1$  has all the Mn-O bond lengths changing uniformly and is defined as  $Q_1 \equiv (Q_x + Q_y + Q_z)\sqrt{2/3}$ . The three-dimensional tetragonal JT distortion mode, commonly known as the  $Q_3$  mode and defined as  $Q_3 \equiv (2Q_z - Q_x - Q_y)/\sqrt{3}$ , has the Mn-O bond lengths changing in all directions [17, 18]. On the other hand, the planar JT distortion mode, commonly known as the  $Q_2$  mode, has the Mn-O bond lengths changing only in the plane and is defined as  $Q_2 \equiv Q_x - Q_y$ . If a single  $e_g$  electron occupies a Mn site, from Eq. (1), it is clear that in the  $d_{z^2}$  orbital the electron would excite both  $Q_1$  and  $Q_3$  modes, whereas in the  $d_{x^2-y^2}$  orbital it would generate only the planar  $Q_2$  excitation.

We will first consider the undoped  $\text{LiMn}_2\text{O}_4$  spinel. As shown in Fig. 1, to minimize energy due to Coulombic interactions, there are two  $\text{Mn}^{3+}$  ions and two  $\text{Mn}^{4+}$  ions in each cube. Furthermore, from the above equation (1) and Fig. 1, it is clear that when only  $d_{x^2-y^2}$  orbital is oc-

cupied by an  $e_g$  electron at a  $\text{Mn}^{3+}$  ion in the  $\text{LiMn}_2\text{O}_4$  spinel, there is no frustration and the energy is minimized. This is because, in any face that is in the  $xy$ -plane of a cube shown in Fig. 1, we have one  $\text{Mn}^{3+}$  ion and one  $\text{Mn}^{4+}$  ion diagonally opposite to each other. Within the above occupancy scenario, only planar  $Q_2$  mode is excited at  $\text{Mn}^{3+}$  sites; then, the distortion at one  $\text{Mn}^{3+}$  site is compatible with the distortion at another  $\text{Mn}^{3+}$

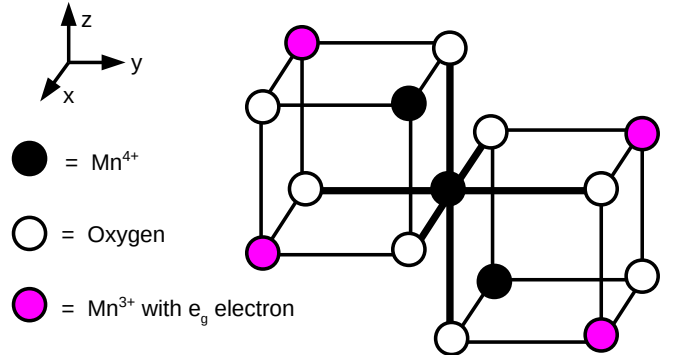


FIG. 1. Part of the unit cell of  $\text{LiMn}_2\text{O}_4$  in an ideal spinel lattice. Octahedral coordination to a manganese is depicted using thicker lines. Each manganese tetrahedron in a cube has two JT-active  $\text{Mn}^{3+}$  ions and two non-JT  $\text{Mn}^{4+}$  ions.

site, thereby cooperatively avoiding frustration. In addition to the BM and JT modes, if other normal modes are also included in our considerations, there may be a slight frustration. In fact, compared to the large JT ordering temperatures (i.e., at least 750 K [19]) in perovskite manganites, the first-order structural transition occurs at a much lower temperature (i.e., about 220 K as shown in Fig. 2) indicating a much weaker frustration due to interaction between cooperative normal-mode distortions. Furthermore, the small overall relative expansion around the structural transition shown in Fig. 2 (which is an order of magnitude smaller than in perovskite manganites [19]) also reflects the relevance of, besides the BM and JT modes, additional cooperative electron-phonon distortion mode(s).

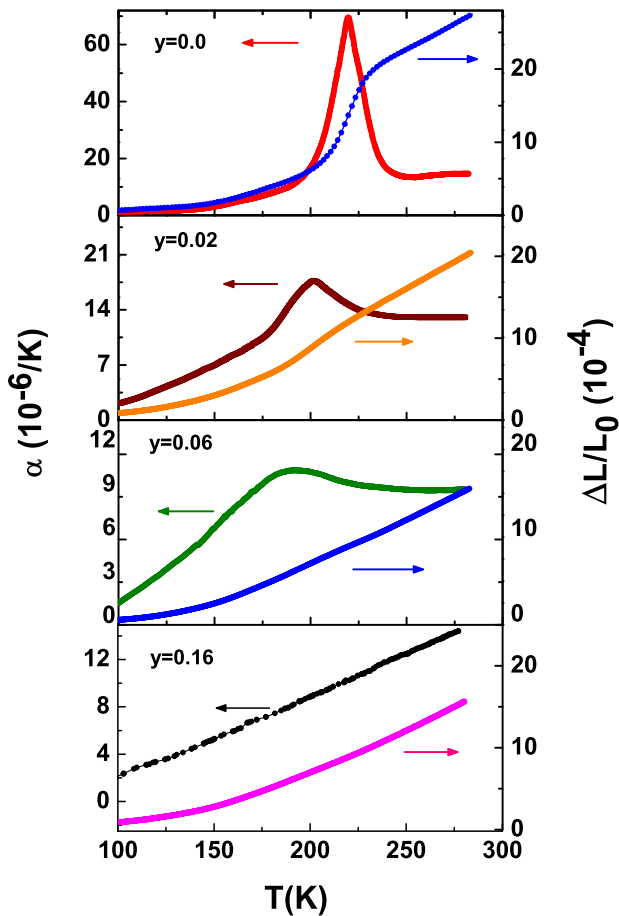


FIG. 2. Thermal expansion measurements on cobalt doped  $\text{LiMn}_2\text{O}_4$ . With increasing doping, there is a decrease in the transition temperature, weakening of the peak in linear thermal expansion  $\alpha(T)$ , and a drop in the relative expansivity  $\Delta L/L_0$  at the structural transition. At a critical doping  $y \sim 0.16$ , the first-order structural transition vanishes due to the forging of a percolating path involving non-cooperative normal modes.

Next, we will analyze the relative expansion  $\Delta L/L_0$  in the doped system  $\text{LiCo}_y\text{Mn}_{2-y}\text{O}_4$ . In the undoped  $\text{LiMn}_2\text{O}_4$ , a structural transition occurs as the temperature is lowered to  $T \sim 220$  K (as shown in Fig. 2) and it indicates onset of cooperative normal-mode distortions. As the doping increases, a fraction of the JT active  $\text{Mn}^{3+}$  (shown in Fig. 1) are replaced by non-JT  $\text{Co}^{3+}$  ions [13, 20]; consequently, the frustration decreases and the cooperative ordering becomes less robust leading to a decrease in the transition temperature of the first-order structural transition. At the structural transition, as can be seen from the plots in Fig. 2, there is a sizeable change in the relative expansivity  $\Delta L/L_0$ ; this change in  $\Delta L/L_0$  diminishes with increasing doping (again illustrating weakening of cooperative ordering) and finally vanishes at a critical doping  $y \sim 0.16$ . At the critical doping  $y \sim 0.16$ , a percolating path involving non-cooperative normal-mode distortions is established. The progressive suppression of the JT transition with Co doping is more clearly visible in the temperature dependence of the coefficient of linear thermal expansion. For undoped sample,  $\alpha(T)$  shows a peak around 220 K; the peak weakens, becomes broader, and shifts to lower temperatures as Co concentration increases and disappears at around  $y=0.16$ .

This picture of weakening cooperative distortions is similar to that observed in systems such as perovskite manganites where the JT ordering temperature diminishes with doping and finally vanishes. A depiction of JT ordering temperature versus doping in  $\text{La}_{1-x}\text{Ca}_x\text{MnO}_3$  is given in Refs. 21 and 22.

Before, discussing conduction in undoped and doped  $\text{LiMn}_2\text{O}_4$ , we will first recapitulate conduction mechanisms in the two-band perovskite manganites and the single-band Holstein model. The crossover from hopping conduction to band-like conduction occurs at lower temperatures in wider-band perovskite manganites such as  $\text{La}_{1-x}\text{Ca}_x\text{MnO}_3$  and  $\text{La}_{1-x}\text{Sr}_x\text{MnO}_3$  [23]. Now, within the two-band picture of perovskite manganites in Ref. [22], the upper broad band (due to undistorted states that are orthogonal to the polaronic states) overlap with the polaronic band to produce conduction at carrier concentrations corresponding to  $0.2 \lesssim x \lesssim 0.5$ . Here, in the case of  $\text{LiCo}_y\text{Mn}_{2-y}\text{O}_4$ , since the hopping integral is smaller than in manganites [24, 25], the upper band is not relevant for conduction. Next, in the single-band Holstein model, band-like conduction occurs when bandwidth is larger than twice the uncertainty in energy due to electron-phonon scattering (i.e.,  $\hbar/\tau$  with  $\tau$  being the scattering time) [26, 27]. However, in the present cobalt-doped  $\text{LiMn}_2\text{O}_4$ , the narrow band width does not produce band-like conduction even at low temperatures and, consequently, only hopping conduction due to a single polaronic band is realized.

We will now discuss the conduction in undoped  $\text{LiMn}_2\text{O}_4$ . Since the  $e_g$  electron at a  $\text{Mn}^{3+}$  site distorts the oxygen cage around it and forms a small polaron (with polaronic energy  $E_p \propto g^2\omega_0$ ) [26, 27], the transport

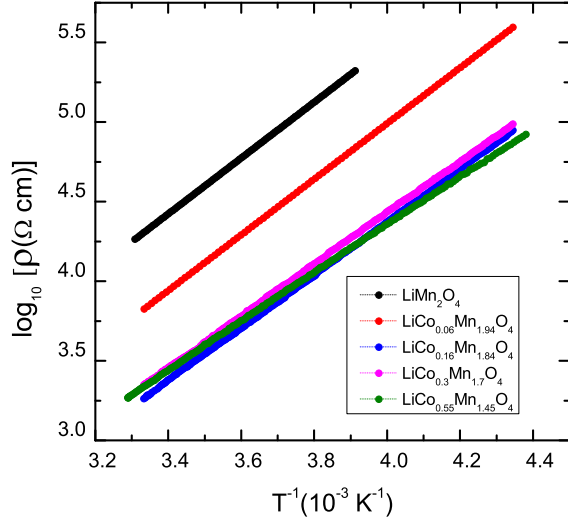


FIG. 3. Linearity in plots of  $\log_{10}(\rho)$  vs  $1/T$  depicting activated transport at various dopings and above the structural transition. For doping below  $y \sim 0.16$ , the resistivity drops sizeably with increase in doping; contrastingly, for  $y \gtrsim 0.16$ , the resistivity does not change much with doping.

of the  $e_g$  electron at higher temperatures (i.e., around room temperature) will be activated with the activation energy  $E_a$  being at least half the polaronic energy  $E_p$ . In fact, the value of  $\frac{(E_a - E_p/2)}{E_p/2}$ , reflects the degree of frustration due to cooperative electron-phonon modes as will be explained below. Now, each  $\text{Mn}^{4+}$  site has four  $\text{Mn}^{3+}$  sites diagonally opposite to it as shown in Fig. 1. If the  $e_g$  electron hops from a  $\text{Mn}^{3+}$  ion to a neighboring  $\text{Mn}^{4+}$  ion, the distortion produced by the remaining three  $\text{Mn}^{3+}$  ions (which are neighbors of the  $\text{Mn}^{4+}$  ion) makes the hopping unfavorable leading to enhancement in the activation energy  $E_a$  by a fraction of the polaronic energy.

Next, we will focus on the conduction in doped  $\text{LiMn}_2\text{O}_4$ . In  $\text{LiCo}_y\text{Mn}_{2-y}\text{O}_4$ , since  $\text{Co}^{3+}$  replaces  $\text{Mn}^{3+}$ , the corners of each cube in Fig. 1 (on an average) are occupied by  $2 - 2y$   $\text{Mn}^{3+}$  ions,  $2y$   $\text{Co}^{3+}$  ions, and two  $\text{Mn}^{4+}$  ions. Since  $\text{Co}^{3+}$  is not JT active, the oxygen-cage surrounding  $\text{Co}^{3+}$  is not distorted. Consequently, hopping from  $\text{Mn}^{3+}$  to  $\text{Mn}^{4+}$  has, on an average, a lower activation energy due to decrease in frustration. The resistivity in  $\text{LiCo}_y\text{Mn}_{2-y}\text{O}_4$  can be expressed as follows [28]

$$\rho = A \frac{e^{(2R/\xi)}}{n} e^{(E_a/k_B T)}, \quad (2)$$

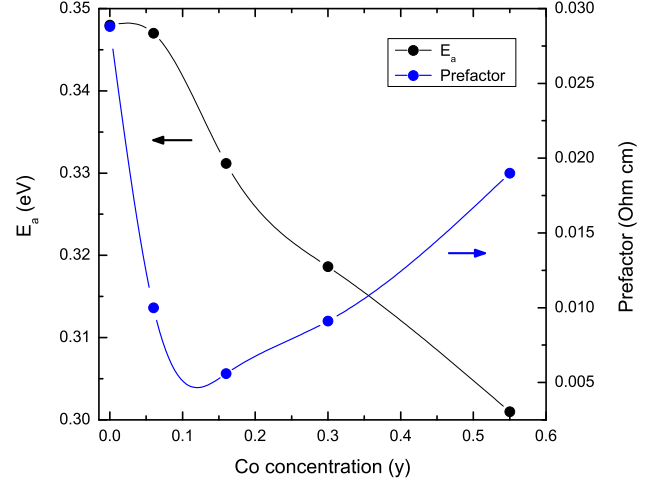


FIG. 4. Plots of the prefactor  $A \frac{e^{(2R/\xi)}}{n}$  and the activation energy  $E_a$  [occurring in the resistivity equation (2)] as a function of cobalt doping in  $\text{LiCo}_y\text{Mn}_{2-y}\text{O}_4$ . The prefactor shows a minimum at  $y \sim 0.16$  and the drop in  $E_a$  is sharper till  $y \sim 0.16$ ; both are indicative of a change in the transport mechanism.

where  $A$  is a constant,  $n$  is the concentration of the mobile  $e_g$  electrons,  $\xi$  is the localization length,  $R$  is the shortest hopping distance for an  $e_g$  electron (i.e., the distance between two neighboring  $\text{Mn}^{3+}$  and  $\text{Mn}^{4+}$  ions), and  $T$  is the temperature. The fact that, even upon doping with cobalt, each  $\text{Mn}^{3+}$  has the same number of diagonally opposite  $\text{Mn}^{4+}$  ions for the  $e_g$  electron to hop to, justifies using a fixed-hopping-distance model rather than a variable-hopping-range model. Our transport model is clearly verified by Fig. 3 which depicts linear plots of  $\log_{10}(\rho)$  versus  $1/T$ . Using Fig. 3, at various Co-doping values, we extract the prefactor  $A \frac{e^{(2R/\xi)}}{n}$  and the activation energy  $E_a$  [occurring in Eq. (2)] and generate Fig. 4. Now, the localization length  $\xi$  decreases with the cobalt doping. Hence, in the above expression for resistivity, the prefactor  $A \frac{e^{(2R/\xi)}}{n}$  will have a minimum as a function of Co-doping because  $\frac{1}{n}$  decreases with doping while the term  $e^{(2R/\xi)}$  increases with doping. In fact, as depicted in Fig. 4, the minimum in the prefactor  $A \frac{e^{(2R/\xi)}}{n}$  occurs at  $y \sim 0.16$ . Here it should be pointed out that, below  $y \sim 0.16$ , localization length decreases slowly with doping (due to cooperative normal-mode-network weakening with doping); whereas above  $y \sim 0.16$ , localization length decreases more rapidly with doping. Next, the activation energy  $E_a$  (as shown in Fig. 4) monotonically decreases with doping; however, the drop is sharper till  $y \sim 0.16$ . Lastly, it is of interest to note that the resistivity drops sizeably with increasing doping until the doping-level attains a value  $y \sim 0.16$ ; at higher doping values (i.e.,  $y \gtrsim 0.16$ ), the resistivity does not change

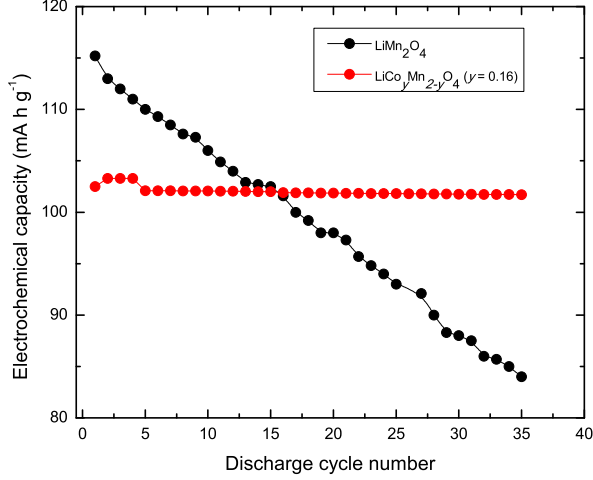


FIG. 5. Electrochemical capacity versus discharge cycle number (adapted from Ref. 29). Capacity fades with repeated cycling for the undoped cathode whereas it remains unchanged at  $y \sim 0.16$ . See Fig. 6 for corroborative doping dependence of capacity.

much (as can be seen in Fig. 3). This can be understood in terms of a non-cooperative network being established at  $y \sim 0.16$ ; this network leads to an enhanced conduction since hopping does not generate unfavorable distortions.

Finally, we will discuss capacity fading as displayed in Figs. 5 and 6. In the undoped case and at lower dop-

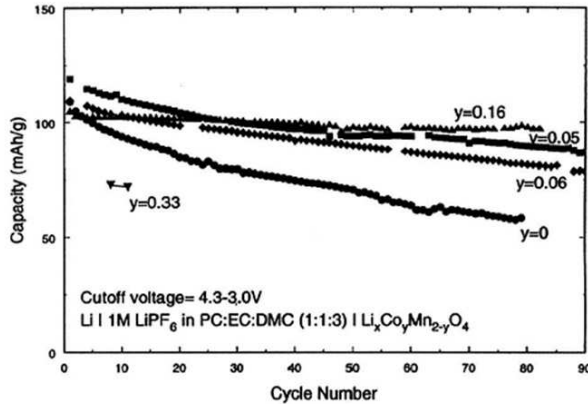


FIG. 6. Variation of the capacity as a function of cycle number for Li/LiCo<sub>y</sub>Mn<sub>2-y</sub>O<sub>4</sub> cells at various cobalt dopings. At higher doping  $y \sim 0.16$ , capacity remains unchanged after repeated cycling. Reproduced from Ref. 11.

ings (i.e.,  $y < 0.16$ ), the network of cooperative/coherent normal-mode distortions restricts lithiation (delithiation) of the cathode material Li<sub>x</sub>Mn<sub>2</sub>O<sub>4</sub>; consequently, each time only a fraction of the un-lithiated (lithiated) material gets lithiated (delithiated). On increasing the doping to  $y \gtrsim 0.16$ , a network of non-cooperative normal-mode distortions is established which facilitates both the lithiation and the delithiation processes. Thus, while there is capacity fading upon repeated cycling at lower values of doping (i.e.,  $y < 0.16$ ), the capacity remains constant for  $y \gtrsim 0.16$ . However, for  $y \gtrsim 0.16$ , at higher doping values the capacity is less due to decrease in the number of carriers. Thus ideally, it is best to use LiCo<sub>y</sub>Mn<sub>2-y</sub>O<sub>4</sub> at  $y \sim 0.16$  for optimal electrochemical performance.

#### IV. CONCLUSIONS

From the results of the thermal expansion and electrical conductivity measurements on LiCo<sub>y</sub>Mn<sub>2-y</sub>O<sub>4</sub> spinel, within the framework of coherent normal-mode physics, we provide an explanation for the optimum doping level that generates best capacity performance in Li/LiCo<sub>y</sub>Mn<sub>2-y</sub>O<sub>4</sub> cells. At  $y = 0$ , the material shows a first-order phase transition attributed to cooperative normal-mode distortions. These cooperative distortions lower the electrical conductivity as well as the efficiency of Li insertion and de-insertion into the spinel structure, leading to lowering of discharge capacity with cycle number. With increase in the doping ' $y$ ', the cooperative-normal-mode network starts to weaken, and at  $y \sim 0.16$  the cooperative network is completely broken. Any further increase in ' $y$ ', only causes a lowering of the capacity due to a decrease in the number of charge carriers. The  $y \sim 0.16$  is thus the ideal doping level for realizing stable discharge capacity of the battery.

#### V. ACKNOWLEDGEMENTS

S. Y. acknowledges stimulating discussions with P. B. Littlewood, M. M. Thackeray, H. Iddir, and J. W. Freeland. The authors thank A. Ghosh for help with the figures and the students of P. Mandal for help with the measurements.



- 
- [1] J. M. Tarascon and M. Armand, *Nature* **414**, 359 (2001).
  - [2] B. L. Ellis, K. T. Lee, and L. F. Nazar, *Chem. Mater.* **22**, 691 (2010).
  - [3] J. B. Goodenough and Y. Kim, *Chem. Mater.* **22**, 587 (2010).
  - [4] L. Croguennec and M. R. Palacin, *J. Am. Chem. Soc.* **137**, 31403156 (2015).
  - [5] D. Larcher and J. M. Tarascon, *Nature Chem.* **7**, 19 (2015).
  - [6] M.M. Thackeray, P.G. Bruce, J.B. Goodenough, *Mater. Res. Bull.* **18**, 461 (1983).
  - [7] See M. Wakihara, G. Li, and H. Ikuta, in *Lithium ion batteries: fundamentals and performance*, edited by M. Wakihara and O. Yamamoto (Wiley-VCH, New York, 1998).
  - [8] L. Guohua, H. Ikuta, T. Uchida and M. Wakihara, *J. Electrochem. Soc.* **143**, 178 (1996).
  - [9] S.H. Wu and H.J. Su, *Mater. Chem. Phys.* **78**, 189 (2002).
  - [10] H. Huang, C. Wang, W.K. Zhang, Y.P. Gan, and L. Kang, *J. Power Sources* **184**, 583 (2008).
  - [11] P. Arora, B.N. Popov, and R.E. White, *J. Electrochem. Soc.* **145**, 807 (1998).
  - [12] C.H. Shen, R.S. Liu, R. Gundakaram, J.M. Chen, S.M. Huang, J.S. Chen, C.M. Wang, *J. Power Sources* **102**, 21 (2001).
  - [13] N. Amdouni, F. Gendron, A. Mauger, H. Zarrouk, C.M. Julien, *Mater. Sci. and Eng. B* **129**, 64 (2006).
  - [14] J. B. Goodenough, *Chem. Mater.* **26**, 820 (2014).
  - [15] J.R.Carvajal, G. Rousse, C. Masquelier and M. Hervieu, *Phys. Rev. Lett.* **81**, 4660 (1998).
  - [16] Ravindra Pankaj and Sudhakar Yarlagadda, arXiv:1608.06055.
  - [17] P. B. Allen and V. Perebeinos, *Phys. Rev. B* **60**, 10747 (1999). Here, electron-phonon interaction is expressed in a different basis.
  - [18] Daniel I. Khomskii, *Transition Metal Compounds* (Cambridge University Press, 2014).
  - [19] Tapan Chatterji, Francois Fauth, Bachir Ouladdiaf, P. Mandal, and B. Ghosh, *Phys. Rev. B* **68**, 052406 (2003).
  - [20] M. Wakihara, *Mater. Sci. and Eng. R* **33**, 109 (2001).
  - [21] see K.H. Kim, M. Uehara, V. Kiryukhin and S.-W. Cheong, in *Colossal Magnetoresistive Manganites*, edited by T. Chatterji, (Kluwer Academic, Dordrecht, 2004).
  - [22] T. V. Ramakrishnan, *J. Phys.: Condens. Matter* **19**, 125211 (2007).
  - [23] E. Dagotto, T. Hotta, and A. Moreo, *Physics Reports* **344**, 1 (2001).
  - [24] M. Atanasov, J.-L. Barras, L. Benco, and C. Daul, *J. Am. Chem. Soc.* **122**, 4718 (2000).
  - [25] R. Basu, C. Felser, A. Maignan and R. Seshadri, *J. Mater. Chem.* **10**, 1921 (2000).
  - [26] Sudhakar Yarlagadda, *Phys. Rev. B* **62**, 14828 (2000).
  - [27] T. Holstein, *Ann. Phys. (N.Y.)* **8**, 343 (1959).
  - [28] N. F. Mott, *Metal-Insulator Transitions* (Taylor and Francis, London/Philadelphia, 1990).
  - [29] K. Ragavendran, L. Lu, B.J. Hwang, K. Barner, and A. Veluchamy, *J. Phys. Chem. C* **117**, 3812 (2013).